ELSEVIER

Ultramicroscopy 81 (2000) 203–222

ultramicroscopy

www.elsevier.nl/locate/ultramic

Zero-loss image formation and modified contrast transfer theory in EFTEM

Isabel Angert, Endre Majorovits, Rasmus R. Schröder*

Max-Planck-Institute for Medical Research, Department of Biophysics, Jahnstrasse 29, D-69120 Heidelberg, Germany

Received 28 July 1999; received in revised form 4 October 1999

Dedicated to Professor Harald Rose on the occasion of his 65th birthday

Abstract

For a weak phase/weak amplitude object the information transfer in the imaging process of TEM is described by the common formalism of the contrast transfer function (CTF). So far the effects of inelastic scattering were not accounted for in this formalism. In conventional imaging they were simply neglected. In energy filtering TEM (EFTEM), where removal of inelastic electrons leads to higher specimen contrast, they were modelled by a global increase of the elastic amplitude contrast. Thus, the description of inelastic and elastic scattering was mixed. Here a new ansatz is proposed which treats elastic and inelastic contrast transfer separately by adding an inelastic contribution to the scattering potentials. In EFTEM this has the effect of adding a filter contrast which depends on the characteristics of the inelastic scattering. For samples with dominant plasmon loss the additional filter contrast is restricted to low resolution. Because of its strong dependence on the nature of the inelastic scattering process, the filter contrast cannot in general be unified with the conventional elastic amplitude contrast.

The modified CTF theory for EFTEM was tested experimentally on a variety of samples. Images of amorphous layers of copper, aluminium, and carbon films, as well as zero-loss images of proteins embedded in amorphous ice were evaluated. The values of the parameters of the additional filter contrast were determined for carbon film and proteins embedded in vitrified ice. Comparison of different CTF models used to reconstruct 3D volumes from zero-loss images confirmed that best agreement with the atomic model is attained with the new, modified CTF theory.

Keywords: Zero-loss imaging; EFTEM; CTF; Filter contrast

1. Why a modified contrast transfer function theory for EFTEM

The validity of an object's reconstruction from its TEM images critically depends on the general understanding of image contrast formation. This is equally true for high-resolution visualization of atoms in solid-state specimens and for low-resolution molecular structure determination of biological samples. Over the years a well-founded theoretical description of elastic and inelastic image formation has been developed, mathematically modelling the contrast transfer in the EM in the form of the contrast transfer function (CTF).

* Corresponding author.

0304-3991/00/$ - see front matter
PII: S0304-3991(99)00190-4

Such transfer functions have been presented for both, idealized elastic bright field imaging, assuming elastic interactions only, and pure inelastic imaging as it is realized, e.g. using energy filtering TEM (EFTEM). For conventional TEM bright field imaging the situation is more complicated: Depending on the atomic composition of the sample a large fraction of electrons is scattered inelastically. Therefore, image contrast is formed by a combination of elastic and inelastic interactions. For the ideal elastic imaging (zero-loss imaging mode with an infinitesimal energy window) the removal of an inelastically scattered part from the incident beam has to be considered. This removal has to result in an additional amplitude contrast (smaller number of particles in the elastic scattering channel, i.e. – in quantum mechanical description – a decreased wave amplitude). Bright field imaging with a finite energy window adds inelastic contributions to the image, resulting in a complicated mixture of elastic and inelastic image contrast.

In conventional contrast theory of bright field imaging, inelastic scattering of the electron wave and its subsequent effects on contrast formation is neglected. This is a good approximation for all samples consisting of elements with high atomic number, i.e. elements with a low ratio of inelastic versus elastic scattering cross-section $\sigma_{\mathrm{inel}}/\sigma_{\mathrm{el}}$. For biological samples, which lack heavy atoms especially when studied in their native, aqueous state using cryo-EM [1,2] the relevance of inelastic scattering for bright field imaging has been studied extensively [3–7]. Despite disagreement among these studies in some details they all indicate the dominance of inelastic scattering. For aqueous biological samples more electrons are scattered inelastically than elastically. Furthermore multiple scattering cannot be neglected since specimen thickness ranges from 50 nm for studies on isolated complexes to 1 μm for tomography of whole cells [8]. Multiple scattering is dominated by inelastic scattering, i.e. almost all multiply scattered electrons have lost energy.

High-resolution structure determination of native biological samples [9–11] or molecular imaging of biological complexes (e.g. for ribosomes [12,13]) has so far not used any object information obtained from inelastic scattering. It was simply neglected or considered to be background adding noise. Similarly, multiple scattering was neglected.

With the availability of EFTEM [14,15], image formation models have to be revised to include inelastic contrast contributions. EFTEM allows the removal of inelastically scattered electrons (zero-loss imaging mode) which above all increases object visibility and SNR [16,17]. This higher object contrast was described as an increased elastic amplitude contrast [18–20]. It is obvious from imaging theory that removal of inelastically scattered electrons cannot be described by an increased elastic scattering potential. Instead an inelastic absorption potential must be added. Such a potential also provides spatial object information in the form of the spatial localisation of the inelastic scattering centres (i.e. atomic electrons) [21–23]. On the other hand the resolution of the resulting inelastic images then depends on the delocalisation of the inelastic scattering process. For intraatomic electron excitation the localisation remains well defined (characteristic ionisation localized within the atomic radius), while e.g. for plasmon excitation it spreads over a nm range.

An image formation theory which includes all three, the elastic phase and amplitude contrast plus the contrast formed by inelastically scattered electrons therefore has to account for three independent scattering potentials. The new, inelastic scattering potential not only depends on the atomic inelastic scattering factor (characteristic ionisations) but also on the inelastic scattering of the sample as a bulk specimen (plasmon or even phonon excitations). In most biologically relevant cases plasmon energy loss dominates inelastic scattering and conceals the signal of the characteristic ionization events. This can be deduced from the electron energy loss (EEL) spectra of ice [3,17]. But more complicated situations can be expected for certain organic polymers such as proteins and DNA/RNA. Therefore the spatial dependence of such an inelastic potential might not be known a priori.

Here we present a new ansatz for a modified EFTEM zero-loss-CTF which adds an effective inelastic scattering potential to the conventional scattering theory. To justifiy this formalism the new theoretical filter contrast zero-loss CTFs are

compared with different experimental CTFs. The images used to calculate experimental CTFs were either conventional, unfiltered or zero-loss energy filtered images of thin, amorphous films. A total of more than 200 images were processed and the resulting power spectra were fitted using either conventional or modified CTF formulas. The finite energy dispersion and imaging aberrations of the filter prohibit true zero-loss imaging. Thus we also studied the effect of a finite selective filter aperture of varying size on the proposed filter contrast and used it to quantify object information including spatial information from inelastic scattering. In addition, a preliminary description of the contrast formation of unfiltered images is given.

2. Ansatz for filter contrast and zero-loss CTF

The energy filter of an EFTEM separates electrons according to their energy loss in its energy dispersive plane. Removing electrons in this plane allows the selective imaging of elastically scattered electrons (zero-loss imaging) or electrons with a specified energy loss (inelastic imaging). In the case of zero-loss imaging, the action of the filter unit is equivalent to that of an absorption potential that is simply proportional to the inelastic scattering potential of the sample.

The elastically scattered electron wave can then be described, using a generalized phase shift Φ_{gen}, by

$$\psi_{sc}(\boldsymbol{r}) = \psi_0(\boldsymbol{r})\exp(\mathrm{i}\Phi_{\mathrm{gen}}(\boldsymbol{r})) \tag{1}$$

where

$$\exp(\Phi_{\mathrm{gen}}(\boldsymbol{r})) = \exp(\mathrm{i}\phi_{\mathrm{el}}(\boldsymbol{r}) + \mu_{\mathrm{el}}(\boldsymbol{r}) + \mu_{\mathrm{inel}}(\boldsymbol{r})), \tag{2}$$

$\phi_{\mathrm{el}}(\boldsymbol{r})$ and $\mu_{\mathrm{el}}(\boldsymbol{r})$ denoting the elastic phase and amplitude contrast potential, $\mu_{\mathrm{inel}}(\boldsymbol{r})$ denoting the above described filter absorption potential. In the notation of Eq. (2) ϕ denotes a positive phase potential whereas μ denotes a negative absorption potential. Assuming a weak phase/weak amplitude object as well as weak inelastic scattering – compared to the unscattered part of the electron wave – the generalized phase shift can be reduced to

$$\exp(\mathrm{i}\Phi_{\mathrm{gen}}(\boldsymbol{r})) = 1 + \mathrm{i}\phi_{\mathrm{el}}(\boldsymbol{r}) + \mu_{\mathrm{el}}(\boldsymbol{r}) + \mu_{\mathrm{inel}}(\boldsymbol{r}). \tag{3}$$

After propagation into the back focal plane of the objective lens, the scattered electron wave can be expressed, in terms of the spatial frequency coordinates $\boldsymbol{k}$ as

$$\tilde{\psi}_{\mathrm{sc}}(\boldsymbol{k}) = (\delta(\boldsymbol{k}) + \mathrm{i}\tilde{\phi}_{\mathrm{el}}(\boldsymbol{k}) + \tilde{\mu}_{\mathrm{el}}(\boldsymbol{k}) + \tilde{\mu}_{\mathrm{inel}}(\boldsymbol{k})) \times \exp(-\mathrm{i}W(\boldsymbol{k})). \tag{4}$$

Here $W(\boldsymbol{k})$ denotes the wave aberration

$$W(\boldsymbol{k}) = \frac{\pi}{2\lambda}(C_s\lambda^3k^4 - 2\Delta z\lambda k^2), \tag{5}$$

with the objective lens spherical aberration C_{s}, the electron wavelength λ and the defocus Δz. It should be noted that the effect of the energy filter – which in reality filters out electrons in the projector lens area of the EFTEM – is mathematically "located" at the sample. This is mathematically justified since the filter absorption potential is proportional to the inelastic scattering potential of the object, and since the elastic and the inelastic part of the electron wave can no longer interfere with each other. Even though physically the inelastic part is removed at a later stage the two parts of the electron wave are de facto separated in the object plane.

In the usual approximation of the object as a weak phase/weak amplitude object, this scattered wave can be used to calculate the intensity of an image as

$$\tilde{I}(\boldsymbol{k}) = \tilde{\psi}_{\mathrm{sc}}(\boldsymbol{k}) \otimes \tilde{\psi}^*_{\mathrm{sc}}(\boldsymbol{k}). \tag{6}$$

Calculating the convolution using Eq. (4) and regrouping the terms yields the final formula for the image transform:

$$\tilde{I}(\boldsymbol{k}) = \delta(\boldsymbol{k}) - 2[\tilde{\phi}_{\mathrm{el}}(\boldsymbol{k})\sin(W(\boldsymbol{k})) + \tilde{\mu}_{\mathrm{el}}(\boldsymbol{k})\cos(W(\boldsymbol{k})) + \tilde{\mu}_{\mathrm{inel}}(\boldsymbol{k})\cos(W(\boldsymbol{k}))]. \tag{7}$$

The power spectrum of the image $PS(\boldsymbol{k})$ is then given by the expectation value $\langle\tilde{I}(\boldsymbol{k}) \times \tilde{I}^*(\boldsymbol{k})\rangle$, normally calculated as the squared amplitude of the image transform.

Except for the additional filter absorption term Eq. (7) corresponds to the normal description of the image transform. In the conventional theory of elastic image formation, it is now assumed that the

elastic atomic amplitude scattering factor is proportional to the elastic atomic phase scattering factor, i.e.

$$\tilde{\mu}_{\mathrm{el}}(\boldsymbol{k}) = -A(\boldsymbol{k})\tilde{\phi}_{\mathrm{el}}(\boldsymbol{k}) \equiv -A\tilde{\phi}_{\mathrm{el}}(\boldsymbol{k}). \tag{8}$$

The factor A has been measured for a variety of samples, and the results indicate that the approximation can be applied up to quasi-atomic resolution. In the case of biological specimens typical values of A are in the order of 5–7% as determined from unfiltered images at a resolution of better than 10 Å [24,25].

A similar assumption must now be made for the filter potential. As described above the filter potential derives from the inelastic scattering potential which in principle contains all the spatial object information. At present there are no methods for exact calculation or simulation of inelastic scattering potentials for biological samples embedded in ice. The best simulation program so far seems to be YaMS [26] which still only takes atomic inelastic events into account, neglecting any excitations of delocalized electron bonds.

Information about the spatial frequency characteristics of the filter potential can be deduced from the spatial resolution obtainable from inelastic images. Different groups have studied the resolution at different energy losses reaching from the extreme low loss region (about 3 eV [27]) to the order of 100 eV [28]. In general, the following suggestion emerges from these studies: Inelastic interactions are less localized than interactions involving elastic scattering, leading to lower resolution images of the imaged samples [29,30]. However, depending on the type of specimen and the size of energy loss, both reflecting the nature – i.e. the localization – of the inelastic event, the obtainable spatial resolution varies. Thus, spatial resolutions were reported to be of the order of 2 nm for amorphous carbon film at an energy loss of $\delta E = 7$–200 eV [31], 1.6 nm for fluorophore crystals at an energy loss $\delta E = 3$ eV [27], 8 Å for diamond grains in a ZnS matrix using the surface plasmon excitation at $\delta E = 25$ eV [32], and 3.8 Å for Ba monolayeres in crystaline high-T_c superconductors using the Ba N-edge ($\Delta E = 100$ eV) for imaging [28]. Organic materials with a broad EEL spectrum at the plasmon loss region seem to be limited in resolution, whereas inorganic samples with well-defined excitations (such as surface plasmons or core loss) allow higher resolution.

As was discussed above, it is not yet possible to calculate the exact absorption potential. To obtain a heuristic, experimental form of the filter absorption potential reflecting the spatial resolution of the inelastic scattering, a combination of the elastic phase potential with a Gaussian envelope is assumed. As a possible ansatz we chose

$$\tilde{\mu}_{\mathrm{inel}}(\boldsymbol{k}) = -B\exp\left(-\left(\frac{k}{C}\right)^2\right)\tilde{\phi}_{\mathrm{el}}(\boldsymbol{k}). \tag{9}$$

It is obvious that this ansatz is only one of many possibilities, assuming a correlation between elastic and inelastic image contrast. As will be shown later, this is in fact the case, even though the contrast formation processes in the elastic and inelastic images are different (first order vs. second order in the electron wave function). Further theoretical and experimental work will be necessary to establish a real physical model and a rigorous formula.

As an effective CTF for the zero-loss image contrast in an EFTEM we therefore propose

$$CTF(\boldsymbol{k}) = 2\Bigg(\sin(W(\boldsymbol{k})) - A\cos(W(\boldsymbol{k})) - B\exp\left(-\left(\frac{k}{C}\right)^2\right)\cos(W(\boldsymbol{k}))\Bigg). \tag{10}$$

So far the additional envelope functions of the conventional CTF have been neglected. However, for the comparison with experimental data all envelopes have to be included. The image transform $\tilde{I}(k)$ can be written out in the form of [33,34]

$$I(\boldsymbol{k}) = \mathrm{Obj}(\boldsymbol{k})CTF(\boldsymbol{k}) \times E_{\mathrm{pc}}(\boldsymbol{k}) \times E_{\mathrm{ch}}(\boldsymbol{k}) \times E_{\mathrm{f}}(\boldsymbol{k}) \times E_{\mathrm{eff}}(\boldsymbol{k}) + N(\boldsymbol{k}), \tag{11}$$

where $\mathrm{Obj}(\boldsymbol{k})$ denotes the FT of the object projection, $E_{\mathrm{pc}}(\boldsymbol{k})$ is the envelope function for partial coherence, $E_{\mathrm{ch}}(\boldsymbol{k})$ is the envelope function for energy spread, $E_{\mathrm{f}}(\boldsymbol{k})$ is the detector modulation transfer function, $E_{\mathrm{eff}}(\boldsymbol{k})$ is an envelope function accounting for additional resolution limiting effects, and $N(\boldsymbol{k})$ denotes the FT of noise.

It should be noted that this equation assumes an ideal zero-loss imaging mode, i.e. no inelastically

scattered electrons remain in the recorded image. The performance of present generation commercial EFTEMs is far from this ideal case, delivering medium range energy dispersion of only 1.1 μm/eV [35] combined with second-order (LEO 912 Ω) or third-order (Gatan GIF) imaging aberrations. To image a certain object area without artefacts from electron scattering on the edges of the energy-selective aperture it is still necessary to work with a wider slit of this aperture. Further, to avoid dose consuming alignment of a small slit for work with beam-sensitive samples – such as vitrified biological specimens – a typical energy width of 1.5–2 times the smallest possible window may routinely be used. Realistic "zero-loss" images are therefore mixtures of the elastic images and small contributions from inelastically scattered electrons with low energy loss. In the case of this study electrons with an energy loss of up to 10–15 eV were included.

3. Materials, methods, and data collection

3.1. Preparation of samples

Amorphous layers of carbon with a thickness of 10–60 nm were prepared by evaporating carbon threads in a high-vacuum chamber (Baltec). Layer thickness was monitored comparing the optical density with films measured previously [5]. Amorphous layers of uranium salt were produced by conventional negative staining techniques (layer thickness not measured), whereas layers of copper and aluminium were obtained by melting and evaporating small pieces of metal foil in high vacuum (Baltec).

Layers of protein embedded in amorphous ice with a thickness of 50–100 nm were produced using perforated carbon films prepared as described in Refs. [2,36].

3.2. Data collection and processing

Images of amorphous carbon film were recorded with a TEM JEOL SSF 3000 (at 300 keV at liquid helium temperature) and an EFTEM LEO 912 Ω (at 120 keV at room temperature). With an FEG as electron source, high electron energy (300 keV), a low spherical aberration coefficient of 1.7 mm and specimen cooling with liquid helium, the TEM provided Thon rings up to a resolution of 5 Å, the final resolution depending slightly on defocus. The TEM images were recorded on a $2\,k \times 2\,k$ pixel Gatan slow–scan CCD–camera (pixel size 24 μm) and negative material (Kodak SO163, full strength developer S19) at different magnifications (99 100× and 369 200× for CCD-camera, 69 800× and 260 000× for recording on film) at an electron dose of $20\,e^-/Å^2$. Negative film was digitized using a SCAI scanner (Zeiss, Oberkochen; pixel size 6.99 μm). Images from the EFTEM were recorded on a $1k \times 1k$ pixel Gatan slow-scan CCD-camera (pixel size 24 μm; magnification 109 600×), on negative film and Imaging Plates (Fuji, FDL UR V). The magnification used for film and IP was 82150x. IPs were digitized using a DIBIS scanner micron1 (DIBIS AG, Birkenfeld, Germany; pixel size 25 μm) [37]. The electron source of the EFTEM was a conventional lanthanum-hexaboride cathode (FEI) which, compared with the FEG, gave a lower beam coherence and thus a lower resolution at which Thon rings were detectable.

Images of copper, aluminium, and ice films were taken with the EFTEM only. Metal films were at room temperature, ice layers at $-180°C$, cooled with liquid nitrogen using an Oxford Instruments cryo-transfer system CT 3500Z.

The EFTEM allows the removal of inelastically scattered electrons. The finite energy dispersion and filter aberrations limit the zero-loss filtering, therefore inelastically scattered electrons with an energy loss of 10–15 eV are still present in the images. To study the effect of this non-ideal 'zero-loss' filtering, carbon images were recorded with different selective aperture widths ($\delta E = 7$–15 eV) or without a filter aperture. Zero-loss images of proteins embedded in amorphous ice were recorded on negative film (magnification 52 700×) and Imaging Plates (magnification 80 000×) using a filter width of $\delta E \approx \pm 15$ eV.

All images were processed using the SPIDER image processing package [38,39]. Power spectra were calculated according to Welch [40] and rotationally averaged.

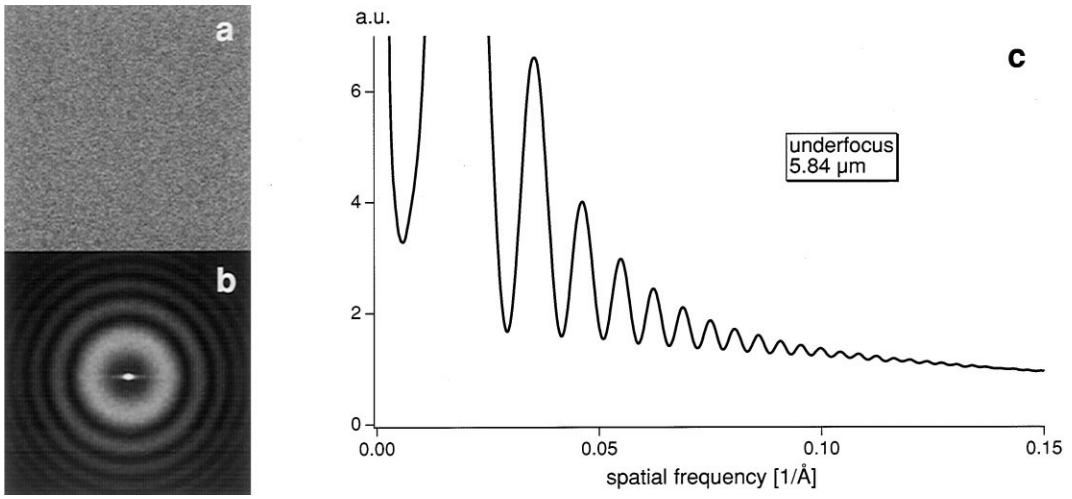

Fig. 1. Image of carbon film recorded at 300 keV with a JEOL SSF 3000 HRTEM, image at 5.84 µm underfocus (a). In (b) an averaged power spectrum with strong Thon rings is shown, and (c) radially averaged profile of the power spectrum (b). The minima of this profile correspond to the transfer zeros of the CTF (cf Eqs. (10) and (11))).

3.3. CTF fitting

Power spectra of images (squared amplitude of image transform) of amorphous material show a strong Thon ring system (Fig. 1), which can be described by Eq. (11). The rings reflect the oscillating characteristics of the CTF with its zero transfer at certain spatial frequencies (Thon ring minima). The positions of the transfer minima and maxima are determined by the microscope parameters (electron energy, objective lens spherical aberration C_s), the image defocus Δf, the ratio parameters for elastic amplitude contrast A, and the filter contrast parameters B and C.

For all experimental data power spectra were calculated and experimental CTFs were fitted according to Eq. (11) in such a way that experimental and theoretical transfer zeros (Thon ring minima) coincide while at the same time minimizing the deviation of zero positions and the general falling off of the Thon ring maxima (fitting of envelope functions). Background correction and CTF fitting were performed using the software package IGOR (WaveMetrics) applying least squares algorithms as described in Refs. [20,33]. In the proposed CTF of zero-loss images (Eq. (10)) the filter contrast is restricted to low resolution as determined by parameter C. Thus in a first step the defocus was determined by fitting the CTF zeros at high resolution (< 12 Å) while the amplitude contrast was kept at $A = 6\%$ for both amorphous carbon and amorphous ice [5,24,25]. In initial fits, the 12 Å threshold was also varied, but, considering the results for inelastic images (cf Fig. 6) it was later kept constant. In a second step the filter contrast and its halfwidth were determined by adjusting the CTF transfer zeros at low resolution. In all fits the spherical aberration coefficient C_s was kept constant (nominal instrument value).

To evaluate the data two processing approaches were applied: In a first step 36 power spectra obtained from images of carbon film recorded at 120 keV in an EFTEM LEO 912 Ω were fitted "blindly", i.e. without knowing whether the particular power spectrum resulted from a zero-loss or an unfiltered image. Out of these 36 power spectra (17 zero-loss and 19 unfiltered) 24 were assigned correctly. Assuming normal distribution statistics this result corresponds to a discrimination between two distinct sets at 90% confidence level. On the one hand this proves a detectable difference between filtered and non–filtered images. However, the 90%

confidence level also shows that a significant number of individual power spectra cannot be assigned correctly, indicating a high variability in the measured positions of the Thon ring minima.

To overcome the large experimental error of individual power spectra an approach assuring high statistics was chosen. Processing a large number of filtered and unfiltered images the corresponding power spectra were all fitted applying Eqs. (10) and (11) using the filter contrast ratio B and spatial frequency halfwidth C as free parameters. Later these individual parameters were averaged.

Fig. 1 illustrates a typical example of experimental data obtained from carbon film. Fig. 1a shows an image of carbon film recorded on CCD at the JEOL SSF3000. The power spectrum with strong Thon rings (Fig. 1b) and its radially averaged profile (Fig. 1c) are used as input for the fitting procedure. Fig. 1c shows the power spectrum before background correction.

For both CTF models (Fig. 2, grey traces) the general damping of the signal as described by the envelope functions in Eq. (11) agrees well with the experimental data after background correction (Fig. 2, black trace). The discrepancy at very low

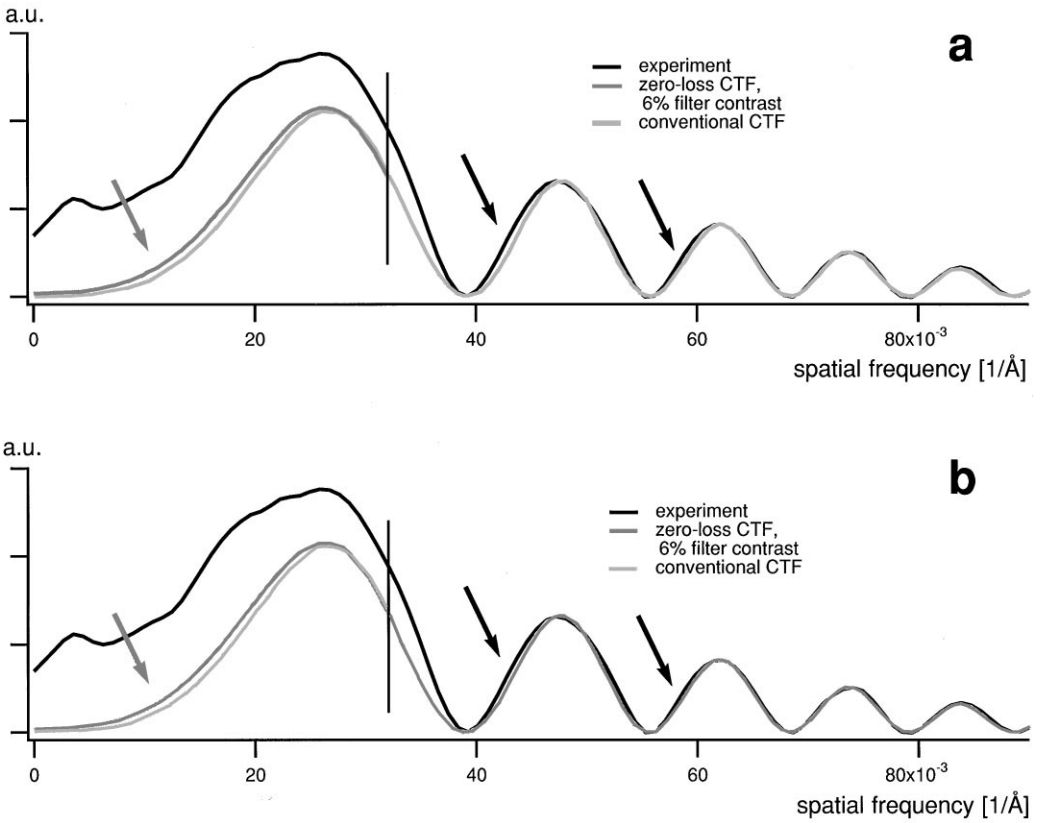

Fig. 2. Comparison between squared theoretical CTFs for the conventional elastic CTF and the proposed zero-loss CTF theory (grey traces) and the background corrected power spectrum profile of a typical experimental image (zero-loss image of carbon film recorded on CCD, black trace). Panels (a) and (b) show the same data, for spatial frequencies higher than 0.03 1/Å only the conventional (a) or the zero-loss profile (b) is plotted. The better fit for the zero-loss CTF theory leads not only to a better agreement in the minima positions (not obvious in the representation chosen here, for this cf. Fig. 7) but to a slightly better fit of the general profile (maxima position, arrows at higher spatial frequencies). Note the difference in signal transfer between the two theoretical CTF theories at low spatial frequency (grey arrow). This difference affects reconstructions when corrected for the CTF effects (cf Figs. 11–13).

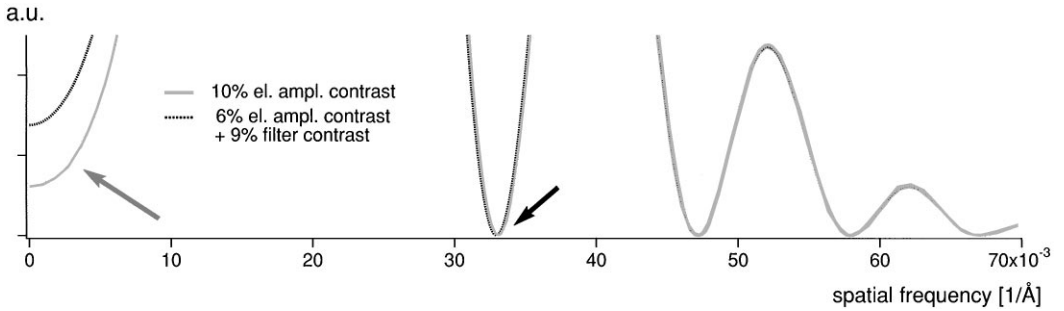

Fig. 3. Comparison between squared theoretical CTFs for the conventional elastic CTF and the new proposed zero-loss CTF theory (shown are curves for a parameter set as obtained from a typical experiment). The positions of the CTF zeros (observed minima) agree well for higher spatial frequencies, only the first minimum is shifted. The signal transfer at low resolution, however, is significantly different for the two different CTF theories. Therefore, a CTF corrected reconstruction will depend strongly in its details on the CTF theory applied (cf Figs. 12 and 13).

spatial frequencies results from the background model used [20]. One difference between the two CTF models is seen in the region of 0.04–0.06 $Å^{-1}$ where the zero-loss CTF fits better to the experimental data.

Note that the main difference between the two CTF models is in the transfer of low spatial frequencies (Fig. 2, grey arrows). This is illustrated further in Fig. 3, which compares the resulting theoretical power spectrum profiles for a conventional elastic CTF with increased elastic amplitude contrast ($A = 10\%$, as found by a conventional fit [20]) and the zero-loss CTF with filter contrast. The transfer minima of the two profiles coincide very well, whereas the zero-loss CTF results in a considerable higher transfer of the low spatial frequency information.

At the FEG-TEM, resolution of imaging was limited by the CCD recording (detectable CTF transfer maxima at about 5 Å). Experimental data recorded on negative film or IP yield similar power spectra, in the case of the EFTEM with sightly lower resolution (detectable CTF transfer maxima to about 8 Å).

4. Experimental results: fitted transfer functions

To verify the proposed form of the zero-loss CTF (Eq. (10)) different experimental proofs are required. These consist of the demonstration (i) that the conventional theory does not describe the data correctly, (ii) that inelastic scattering causes this discrepancy, and (iii) that the new ansatz describes zero-loss imaging of specimens composed of light elements better than previous formalisms. The latter will be illustrated by images of amorphous carbon film and protein embedded in vitrified ice.

4.1. Breakdown of conventional CTF theory

Images of protein embedded in vitrified ice most convincingly indicate the problems with the conventional CTF theory. Fig. 4 shows a typical radially averaged profile of the power spectrum obtained from an individual zero-loss image of tobacco mosaic virus (TMV) embedded in amorphous ice (Fig. 4, black line, image at 3.25 μm underfocus, profile after background correction, cf Eq. (11)).

Fitting of such experimental power spectra based on the conventional elastic theory (i.e. without the newly introduced filter term) leads to an increased elastic amplitude contrast of 10–14% [18–20,33]. These fits keep the elastic amplitude contrast constant over the whole spatial frequency range. The higher SNR of the transfer minima at low spatial frequencies leads to an increased statistical weight of the low frequencies. This results in a misfit of the calculated and experimentally observed minima at higher resolution (shifted CTF minima), as is illustrated for the profile calculated for elastic CTF

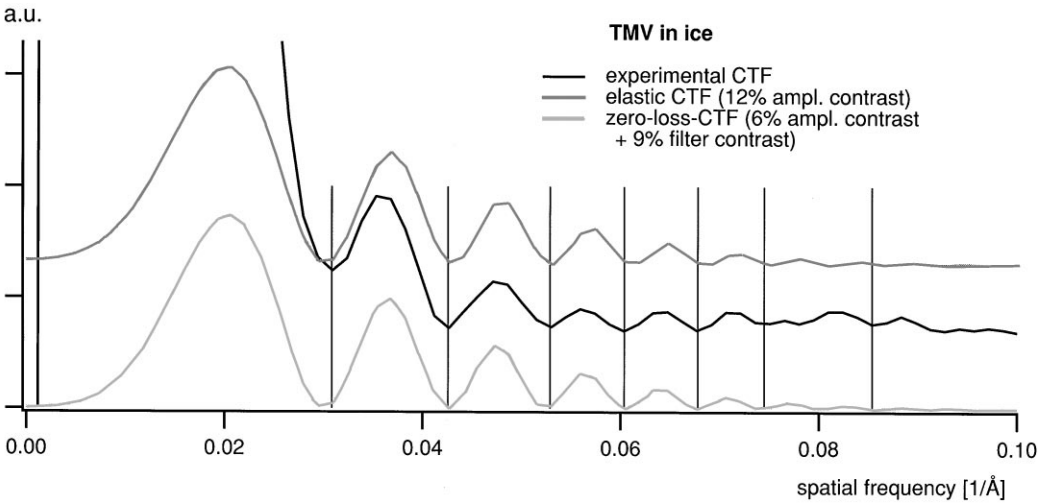

Fig. 4. Radially averaged power spectrum of one single zero-loss image of TMV embedded in ice (black line). The image was recorded with an EFTEM LEO 912 Ω at 120 keV. Best fits for different theoretical CTF models are shown in grey. The overall fit for the conventional elastic CTF is very poor.

parameters in Fig. 4 (dark grey, CTF at 12% elastic amplitude contrast). The attempt to fit all observed minima with equal weights (six observable minima at a resolution of 12 Å) leads to a lower elastic amplitude contrast and an overall unsatisfactory agreement of the zeros [20,33].

This situation contradicts the finding that quantitative CTF correction from zero-loss filtered images of vitrified samples leads to correct density distributions at a higher elastic amplitude contrast of 13–14% [18,19]. These results had been obtained from models at moderate spatial resolutions of 2–3 nm without fitting of CTF transfer zeros.

This conflict – and the need for a quantitative CTF correction to obtain meaningful 3D molecular structure data at lower resolution – calls for a detailed investigation of the spatial dependence of the additional filter contrast. As a first indication a fit using the new zero-loss CTF is included in Fig. 4 (light grey curve), showing good agreement over the full spatial frequency range.

4.2. Validation of weak-phase approximation

The observed shifting of the transfer minima (CTF zeros) for the images of protein embedded in ice (Fig. 4) does not directly show the need for a new CTF theory. In principle such shifts can also be produced by other effects, above all by the violation of the weak-phase approximation. This cannot be excluded a priori since frozen hydrated specimens are usually thicker samples. If a violation of the weak-phase approximation causes the observed shifts of minima, they should be observable for other, strongly scattering objects as well. A thick layer of uranium atoms (uranyl acetate negative stain on carbon film zero-loss recorded with an EFTEM at 120 keV, no objective aperture) was used as a test specimen (atomic number $Z = 92$) for strong elastic scattering.

Fig. 5 shows the experimental and calculated power spectrum profiles. Excellent agreement between experiment and conventional elastic CTF theory is found, i.e. no signs of a possible breakdown of the weak-phase/weak amplitude approximation are present. The strong elastic scattering is only reflected in a high, elastic amplitude contrast of 20%. As the ratio of elastic and inelastic scattering cross–section can be approximated by $\sigma_{\mathrm{inel}}/\sigma_{\mathrm{el}} \approx 18/Z$ [41], uranium scattering is dominated by elastic scattering, i.e. about five times more electrons are scattered elastically than inelastically.

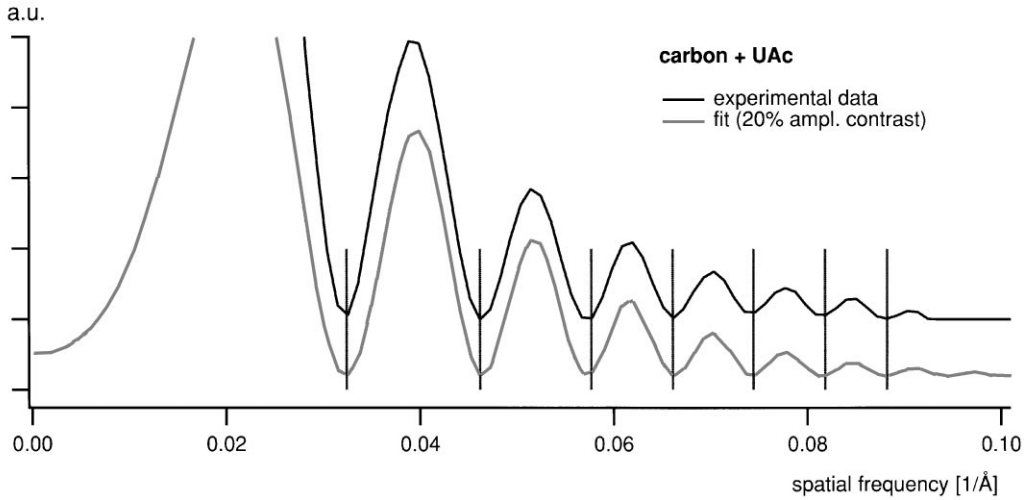

Fig. 5. Radially averaged power spectrum of one single image of an amorphous layer of uranium atoms (negative stain on carbon film). The image was recorded unfiltered with an EFTEM LEO 912 Ω at 120 keV. The fitted CTF was calculated applying the conventional elastic CTF theory.

This strongly suggests that the observed shifts of the minima for organic material embedded in ice result from inelastic scattering.

4.3. Shifting of CTF minima depends on atomic number

To further prove the dependence of the shifts of CTF zeros on inelastic scattering, a simple experiment was performed with amorphous layers composed of elements with different atomic number Z. Filtered–unfiltered pairs of images were recorded and their power spectra fitted individually. The differences in the minima positions of the profiles (CTF transfer zeros) were calculated from the fits. Fig. 6 shows these positional differences for images of copper ($Z = 29$), aluminium ($Z = 13$) and carbon ($Z = 6$).

Images were recorded as a filtered–unfiltered pair at the same defocus. For this experimental setup the defocus stability of the EM was tested by exposure series over a long time range (60 min), which showed some defocus variability. However, the observed variability is small and cannot explain the observed shifts of CTF zeros in filtered–unfiltered pairs.

Comparing the CTF zeros for unfiltered versus zero-loss images a global shift of zero positions, resulting from a change in defocus, has to be distinguished from noticeable systematic deviation of minima positions. For copper and aluminium a global shift is found which can be explained by a slight change in defocus. For carbon the effect is different. At high resolution (better than 10 Å) the shift of positions is unidirectional, a result of defocus variation. For low resolution, however, the minima are shifted in the other direction, i.e. it looks as if one Thon ring system is expanded with respect to the other. As for protein in ice (Fig. 4), it is not possible to fit the shifted CTF zeros using the normal elastic CTF theory.

It should be noted that the copper film data prove once again the validity of the weak-phase/weak-amplitude approximation (Section 4.2). The power spectra of the pair can both be fitted with conventional elastic CTF theory with an amplitude contrast of 12%.

The results presented in Fig. 6 give evidence of a Z-dependent zero-loss CTF: For elements with low atomic number inelastic interactions dominate scattering. At the same time an experimental zero-loss CTF is found where spatial frequency depend-

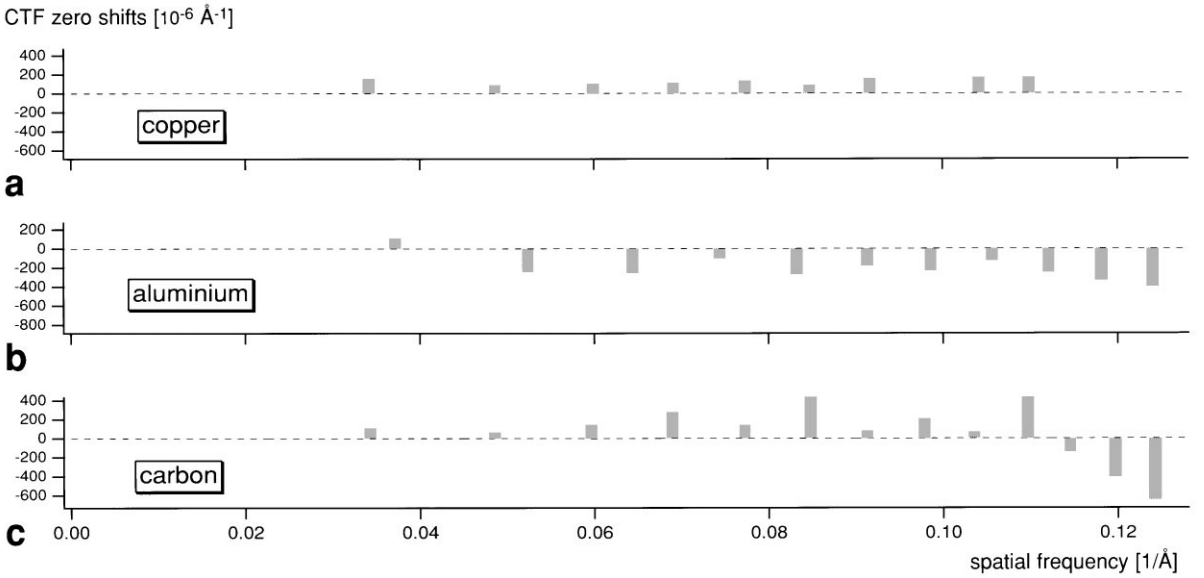

Fig. 6. Differences of CTF zero positions (power spectra minima) between unfiltered and zero-oss filtered images of amorphous films of copper (a), aluminium (b) and carbon (c). Images were recorded with an EFTEM LEO 912 Ω at 120 keV. In the case of copper ($Z = 29$) the differences observed can be explained by a global change in the image defocus (all differences positive). For aluminium ($Z = 13$) and even more so for carbon ($Z = 6$) a local shift of the minima is found (negative difference for high resolution, (more) positive at lower resolution).

ence of the zero positions cannot be described with the elastic scattering potentials. Thus a Z–dependent, inelastic, and frequency dependent scattering potential must be included.

4.4. Amorphous carbon layers as proof for zero-loss CTF

To verify the analytical form of the zero-loss CTF, filtered and unfiltered images of amorphous carbon film were processed. Scattering by carbon atoms is the ideal model case as it is dominated by inelastic events [5,41]. Furthermore, carbon is one of the most abundant atoms in organic material, therefore carbon film is the ideal sample to test the relevance of the proposed CTF for EM of native biological material.

In Fig. 7 the positional differences of CTF zeros between experiment and fit for different possible CTF theories are plotted. Data from unfiltered images are consistent with the conventional elastic CTF (best fit with 0% filter contrast, whereas the best fit for zero-loss data was obtained with the zero-loss CTF at 6% filter contrast (Fig. 7a). In both cases the elastic amplitude contrast was fixed at 6% [24,25]. Fitting the high-resolution region of zero-loss experimental data with a conventional elastic CTF, however, leads to a systematic, global misfit of zeros (Fig. 7b). This illustrates that fitting of data with the inappropriate CTF model (filtered with conventional elastic CTF, unfiltered with zero-loss CTF) gives an unsatisfactory overall fit of the minima positions. An exceptional situation is found for the first minimum of the experimental zero-loss CTF which always seems to be shifted to spatial frequencies higher than expected from theory.

The examples in Fig. 7a also demonstrate the experimental positional error of individual records (fluctuation around zero difference). To overcome this experimental error 117 images of amorphous carbon film were processed. Images were unfiltered or zero-loss energy filtered with energy windows of $\delta E = \pm 7.5, 10, 15$ eV. Their CTF parameters were then averaged within these energy window sets and the resulting parameters are given in Table 1.

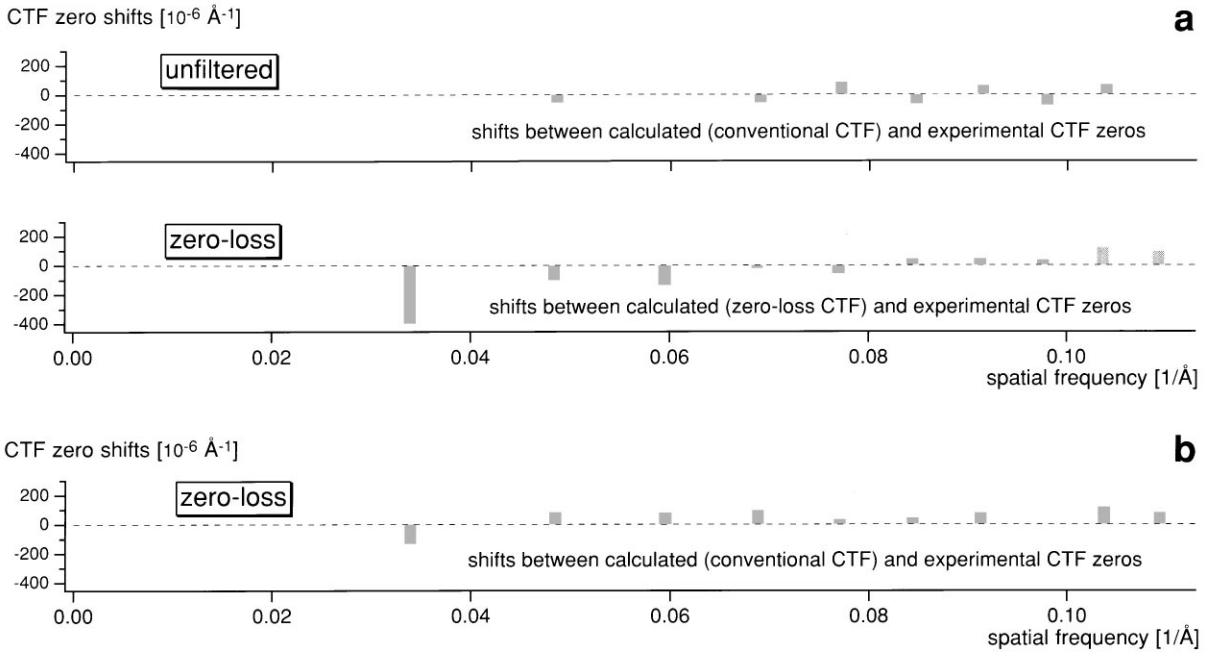

Fig. 7. Differences of CTF zero positions (power spectra minima) between experimental and fitted power spectrum profiles for unfiltered and zero-loss filtered images of carbon film recorded at 120 keV with an EFTEM LEO 912 Ω, energy window width $\Delta E = 15$ eV. (a, upper panel) shows the fit of the conventional elastic CTF to the unfiltered data. A good agreement is obvious (observed differences represent the typical experimental errors in the determined zero positions). Similarly, the fit of the proposed zero-oss CTF to zero-loss filtered experimental data is shown in (a, lower panel). Again, the residual differences vanish on average, except for the first zero position, which cannot be fitted. (b) shows a systematic, in this case positive, shift between experimental and theoretically expected zero positions when the conventional elastic CTF model is used to fit zero-loss data.

Table 1
Filter contrast ratio parameter B and spatial frequency half-width parameter C as obtained from averaging 117 images of amorphous carbon film recorded with an EFTEM at different energy filter widths ΔE (for the definition of B, C see Eq. (9)). As expected, the filter contrast decreases with wider energy window. The value of parameter B for the unfiltered images is consistent with a vanishing filter contrast. The large standard deviation illustrates the large experimental error of single CTF fits

	$\Delta E = \pm 7.5$ eV	$\Delta E = \pm 10$ eV	$\Delta E = \pm 15$ eV	Unfiltered
B (%)	10.4 ± 5.4	6.0 ± 2.2	4.06 ± 1.95	4.83 ± 3.25
C (Å)	22.6 ± 5.9	20.9 ± 3.3	21.8 ± 4.9	22.9 ± 5.1

The largest amount of filter contrast ($B = 10.4 \pm 5.4\%$) was found for the smallest energy filter width ($\delta E = 7.5$ eV). With increasing filter width the amount of filter contrast decreases to $B = 4.06 \pm 1.95\%$ for $\delta E = 15$ eV. This behaviour simply reflects the decreasing number of electrons removed by the wider slit aperture. The parameters found for the unfiltered images are in fact consistent with a vanishing, or very small filter contrast, i.e. the zero positions could just as well be described approximately by the elastic scattering theory.

The averaged halfwidth C of the filter contrast was found to be on the order of 21 Å independent of the filter width. This indicates that filter contrast is restricted to low resolution as is expected from

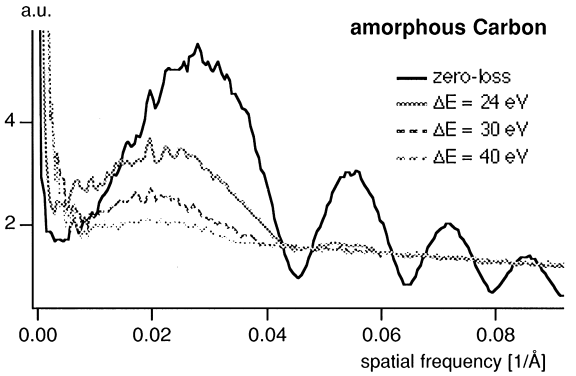

Fig. 8. Radially averaged power spectrum of zero-loss and inelastic images of amorphous carbon film. Images were recorded with an EFTEM LEO 912 Ω at 120 keV. The energy window width for the filtering was ± 15 eV for the zero-loss image and ± 7 eV for the inelastic images. Thon rings are clearly seen for the inelastic images.

a plasmon dominated inelastic scattering potential. To verify this finding inelastic images of carbon films recorded at 120 keV at different electron energy losses were processed. Fig. 8 shows the different radially averaged power spectra. The experimental power spectra of the inelastic images clearly show Thon rings. This can be explained by multiple, elastic–inelastic scattering: Consider an electron scattered first inelastically and then elastically. According to quantum mechanics, after the first process both its energy and its direction are no longer well defined, instead probability distributions have to be assumed. Since the inelastical scattering process is a virtual source for an electron wave, this new wave has a large energy spread and low spatial coherence. Therefore, the envelope functions E_{ch} and E_{pc} are damping the transfer functions rapidly with increasing spatial frequency. As shown in Fig. 8 the elastic signal does not extend beyond 15–20 Å, illustrating that with increasing energy loss the obtainable spatial resolution decreases. This resolution limit is in good agreement with the halfwidth of 21 Å derived from CTF fitting.

4.5. Image contrast in unfiltered images

The data from unfiltered carbon film indicate that the elastic theory might not be sufficient to describe contrast formation of unfiltered images. It is clear that an unfiltered image is the superposition of a zero-loss filtered image with the corresponding inelastic image. Thus the real image intensities are far from those of a hypothetical pure elastic image. However, as is shown in Fig. 9, the inelastic image does in part compensate the contrast produced by the removal of inelastically scattered electrons, i.e. inelastic image contrast and filter contrast cancel each other out under certain conditions and for certain spatial frequencies.

To illustrate this effect the simulation program YaMS [26] was used to calculate images for the parameters of the two TEMs used in our study (an infinite coherence was assumed for these simulations). The chromatic defocus effects depend on the ratio of inelastic energy loss to initial electron energy $\Delta E/E_0$. A good approximation of the non-chromatic EM is therefore a high-voltage TEM. With such a microscope defocus effects on the inelastic images are minimized. Figs. 9a and e show the simulated purely elastic images of the bacteriorhodopsin trimer at 100 nm underfocus (atomic model from pdb-coordinates).

Including inelastic scattering into the simulations leads to general changes in the image contrast. In particular, specimen contrast in the zero-loss filtered image is increased (data not shown). This additional contrast, corresponding to our filter contrast, is visualized as a difference image (zero-loss minus purely elastic image) in Figs. 9b and f. Compared to these images the inelastic images in Figs. 9c and g (without blurring due to chromatic aberration) or in Figs. 9d and h (realistic inelastic images) have reversed contrast but correlating spatial information. Since image contrast in elastic and inelastic images is formed by different physical processes its compensation is not perfect. Fig. 9i shows the Fourier ring correlations between filter contrast image (Figs. 9b and f) and inelastic image (Figs. 9d and h). For the 120 keV TEM the correlation breaks down at a resolution of about 2 nm, at a lower resolution, however, image contrast is perfectly reversed. For the high-voltage TEM the resolution range with perfectly reversed image information extends to about 8 Å resolution.

If contrast reversal were perfect the image contrast observed in an unfiltered image would be just

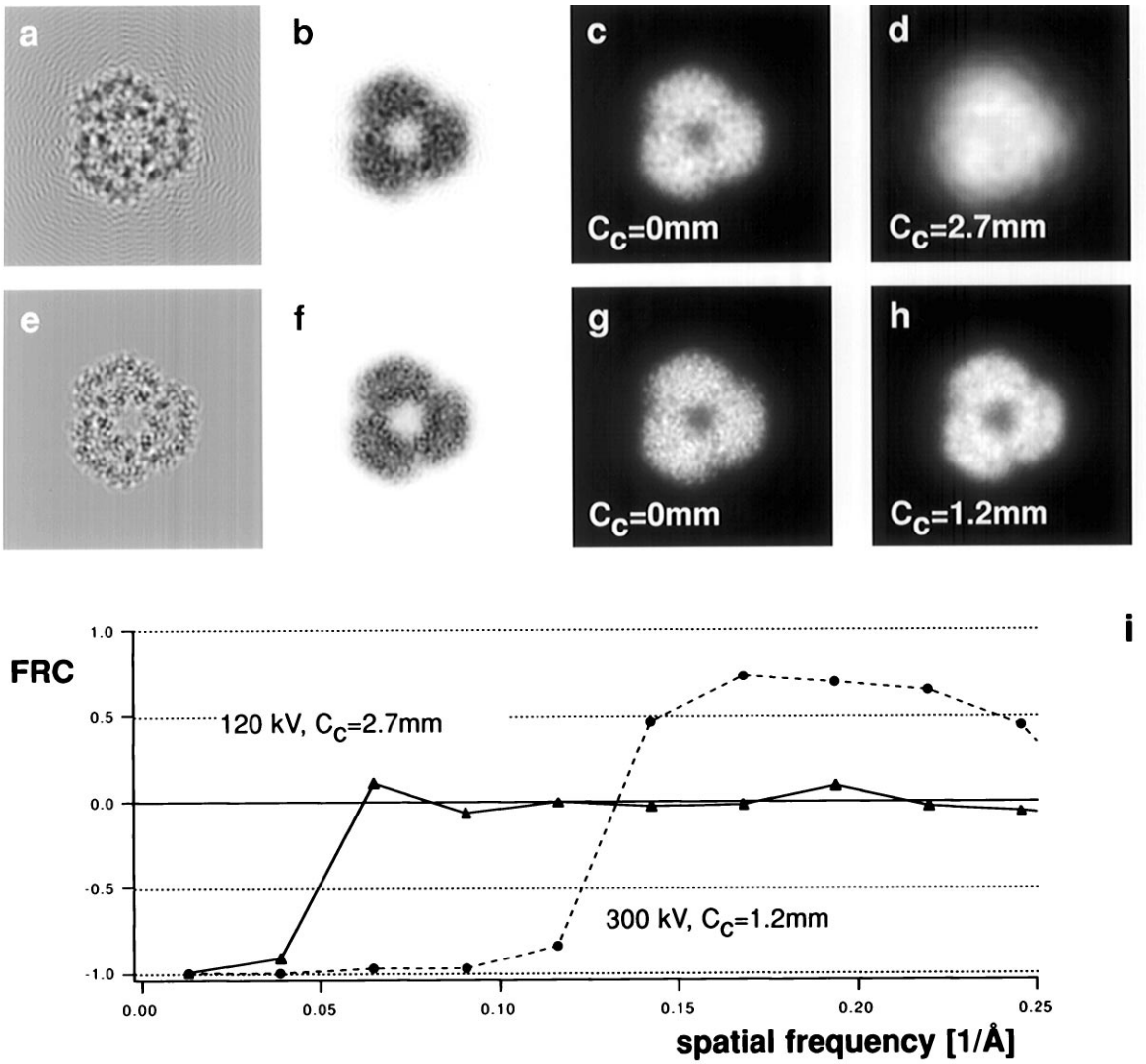

Fig. 9. Correspondence between elastic and inelastic images simulated with the program YaMS Mueller. The imaging situations of a typical 120 kV TEM ($C_s = 2.7$ mm) (a–d) and a 300 kV high voltage TEM ($C_s = 1.2$ mm) (e–h) are compared: A bacteriorhodopsin trimer (pdb-atomic coordinates) is displayed as ideal elastic image (a and e) or as a difference image (zero-loss image minus elastic image, b and f). The contrast in the difference image is equivalent to the elastic object contrast (cf. a–b, e–f), i.e. it is an additional filter amplitude contrast image of the object. The inelastic images for vanishing chromatic aberration ($C_c = 0$ mm, c and g) or a typical real value ($C_c = 2.7$ mm/1.2 mm, d and h) are of reversed contrast to the bright field images and are blurred by aberration effects. Figure (i) shows the Fourier ring correlation (FRC) between zero-oss filter contrast image (b,f) and the inelastic images (d,h) for the two different TEMs.

the elastic contrast. For the 120 keV TEM this would be the case at low-resolution only, whereas at the 300 keV TEM this extends to high resolution. At highest resolution (better than 8 Å) the different nature of elastic and inelastic image contrast becomes obvious (positive correlation in Fig. 9i) and precludes contrast interpretation.

To conclude, high-voltage TEM provides a very good approximation of pure elastic contrast in normal, unfiltered images. Therefore, the conventional

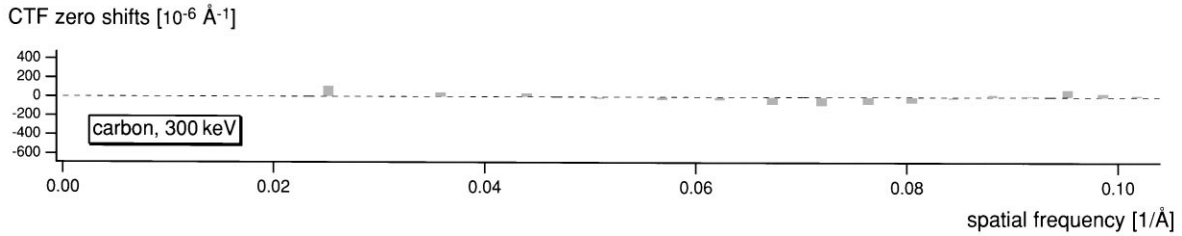

Fig. 10. Differences of CTF zero positions (power spectra minima) between unfiltered images of amorphous films of carbon recorded with a HRTEM JEOL 300 SSF at 300 keV and the conventional elastic CTF model. The fact that the differences vanish for almost the complete spatial frequency range demonstrates the good agreement between experiment and conventional elastic CTF model.

elastic CTF theory should be sufficient to describe image contrast of unfiltered images. Indeed an excellent agreement of experimental with calculated elastic power spectrum minima positions for carbon film is shown in Fig. 10.

5. Protein embedded in amorphous ice, an application

An additional test and a first application of the zero-loss CTF theory is its use in the processing of images of protein embedded in ice. It was stated before that carbon is a good representative atom for biological material. Nevertheless, it is necessary to find the CTF parameters B and C for each specimen individually. This follows directly from the equivalence of filter potential and inelastic scattering potential, which is dependent on the specimen studied. A total of 16 energy filtered images of the actin-myosin complex embedded in ice was processed (ice layer thickness between 50 and 100 nm, electron energy 120 kV, zero-loss energy window width $\delta E \approx \pm 15$ eV). As before the elastic amplitude contrast contribution was fixed at 6% [24], whereas parameters B and C were determined by the fitting of minima positions. The averaged parameter values are $B = 9.5 \pm 3.7\%$ and $C = 20.3 \pm 3.4$ Å. For both, protein in ice and carbon film (Table 1) the halfwidth is of the order of 20 Å. When the EEL spectra of carbon and ice layers [3,41] are compared a dominance of the plasmon peak is found in both spectra, thus it is not surprising that the inelastic scattering potential is equally delocalized. Protein in ice has a higher filter contrast $B_{\text{protein}} = 9.50 \pm 3.67\%$ than carbon $B_{\text{carbon}} = 4.06 \pm 1.95\%$ (for an energy window of 15 eV).

The new zero-loss CTF parameters were then used to correct the CTF when reconstructing the actin–myosin complex: The radial density profile of this filamentous complex changes with defocus and should attain the profile of the atomic model after correction with the appropriate CTF. Fig. 11 illustrates the situation for the atomic model and for images at two typical defocus values. Shown are the projected pdb–model of one helical repeat (13/6 helical complex, Fig. 11a), the averages of 132 single images at 1.6 μm underfocus (Fig. 11b) and of 140 single images at 2.6 μm underfocus (Fig. 11c). The Fourier ring correlation between images in Figs. 11b and c indicates a resolution of 2 nm (data not shown). The calculated 3D volumes are therefore limited to this resolution in Fig. 11d (pdb atomic model), Fig. 11e (1.6 μm data), and Fig. 11f (2.6 μm data). The normal artefacts of reconstructions from images not corrected for the CTF are seen in the reconstructed volumes. The myosin molecule's shape and its density at high radius change strongly with defocus. This is reflected in the projected densities (Figs. 11g–i). A strong difference between atomic model and images is obvious.

The experimental images were then CTF-corrected with a weighted Schiske filter [42], using different sets of CTF parameters for conventional and zero-loss CTF. Fig. 12a shows the resulting projection image calculated for the correction with zero-loss CTF and filter contrast parameter $B = 9\%$ (elastic amplitude contrast fixed at 6%). When different parameter sets and the different formulas for

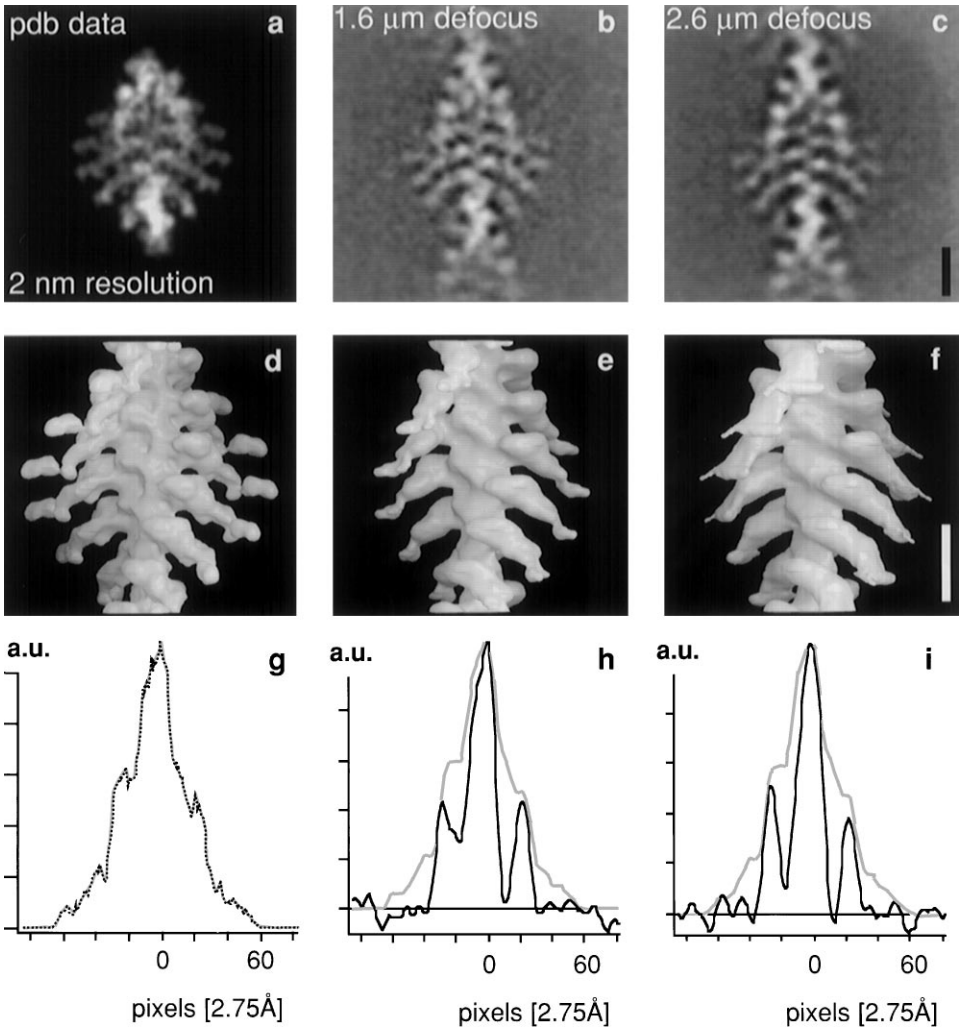

Fig. 11. 2D projections of the atomic model, experimental images, 3D reconstructions and radial density profiles of the actin–myosin protein complex. (a) pdb atomic model of the complex, one helical repeat of the 13/6 helical complex is shown. Single particle averages of experimental images of the complex embedded in vitrified ice are shown for two underfocus values (b) 1.6 µm, (c) 2.6 µm. (d–f) 3D reconstructions of the object images (a–c). (g–i) radial density profiles of images (a–c). (g) The black dotted line represents the profile of the atomic model at 5 Å resolution, the light grey line at 2 nm resolution. (h,i) light grey shows the atomic model as in (g), the black solid lines are the experimental profiles. See text for details.

the CTF are used for the correction the resulting density profiles (from here forth referred to as corrected profiles) change as shown in Fig. 12b.

At first sight the conventional elastic CTF correction seems to reproduce the model density best, although details of the profile are missing. It should be noted, however, that the parameters used for this particular correction do not reproduce the correct CTF minima positions. In fact, this faulty correction produces a wrong density profile: As can be deduced from the original profiles (Fig. 11h,i) the molecular complex was not fully decorated. When the actin densities in the centre (pixel 0) are scaled to the atomic model the integrated myosin densities at higher radius are lower than expected (peaks left and right of the central actin peak). Integrated

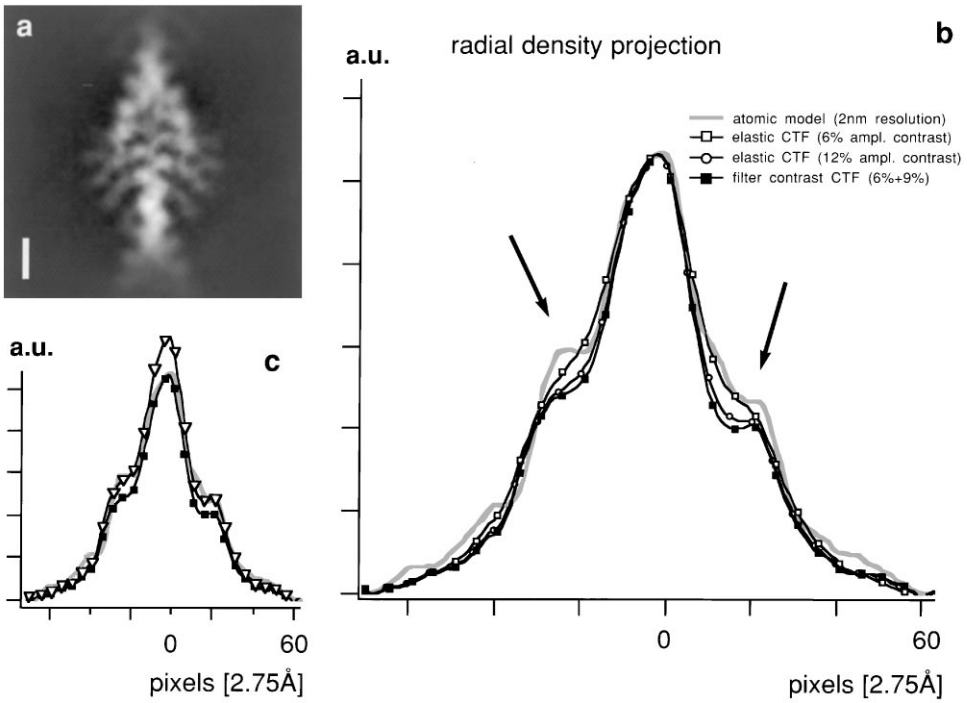

Fig. 12. (a) shows the CTF corrected image of the actin–myosin complex as calculated from the images in Fig. 8b and c. For the correction the proposed zero-loss CTF with 6% elastic amplitude contrast and 9% filter contrast was applied. (b) Density profile for different sets of CTF parameters and CTF theories. The light grey line shows the atomic model profile as in Fig. 8(g). (c) Radial density of the corrected image (a). Two possible scalings are shown to illustrate the fit to the atomic model.

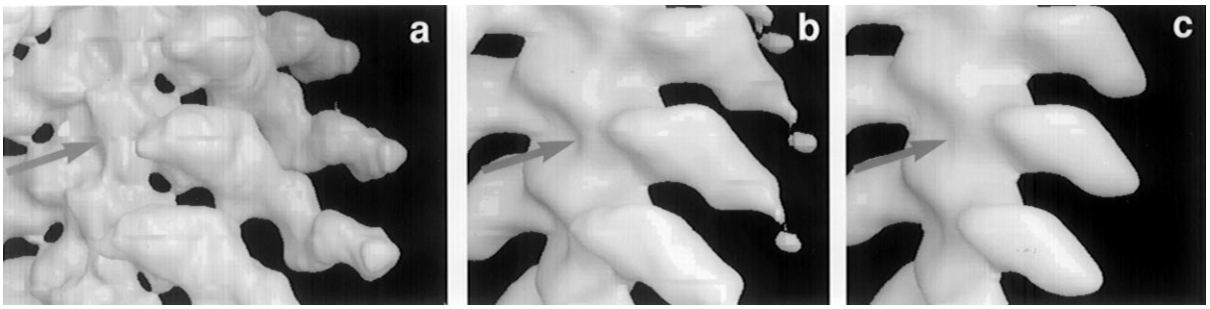

Fig. 13. Comparison between the model 3D density obtained from the atomic pdb-coordinates limited to a resolution of 2 nm (a), experimental reconstruction corrected applying the new proposed zero-loss CTF model (b), and experimental reconstruction corrected applying the conventional elastic CTF model (c). The data in (b) and (c) extend to about 2 nm resolution. The differences in the radial density distribution (visibility of density at high radius) are shown in detail (arrows, connecting bridge between two adjacent actin monomers). These differences result from the different correction factors of structure amplitudes in the low spatial frequency region (meridional structure factors, J_4 Bessel function, respectively; cf. Fig. 3).

density is not affected by CTF effects and can be used directly to scale between uncorrected and corrected projections. This means that after the appropriate CTF correction the myosin density (Fig. 12b, shoulders left and right of central actin peak, arrows) in the corrected profiles has to be lower than in the atomic model (grey trace). This is the case for correction with higher elastic amplitude

contrast [18,19] and with the proposed zero-loss CTF. The details of the profile are remodelled best with the zero-loss corrected profile at a filter contrast of $B = 9\%$ as is shown in Fig. 12c: Here the myosin density is upscaled (black squares → open triangles) and fits well to the atomic model.

The better agreement is reflected in the 3D reconstructions (Fig. 13). Comparing the radial density distribution of the pdb-model volume (Fig. 13a) with the zero-loss CTF corrected volume (Fig. 13b) and the elastic CTF corrected one (Fig. 13c) reveals a profound lack of density and detail in Fig. 13c. This is the effect of a wrong correction of the equatorial structure factor amplitudes in the image transform.

6. Conclusion

Image and contrast formation of samples dominated by inelastic scattering necessitates a new, modified theory of contrast transfer. The data presented here prove that an inelastic absorption potential has to be added to the potentials which describe elastic scattering of the electron wave. For ideal zero-loss imaging this potential can be understood as filter potential, equivalent to an additional amplitude contrast term.

The difference to previous descriptions of the increase in specimen contrast by zero-loss filtering is the clear distinction between elastic and inelastic contrast mechanisms. Whereas formerly the elastic amplitude contrast was simply increased [18,19], an additional scattering potential is introduced here. As has been demonstrated for amorphous carbon film and protein embedded in ice this potential is not proportional to the elastic atomic scattering factors. Instead it falls off at higher resolution, i.e. higher scattering angles. This can be explained by inelastic scattering processes which involve the atomic electrons. For carbon films or ice layers strongly delocalized plasmon electrons could account for the observed decrease of the filter potential beyond 2 nm resolution (filter contrast half-width of the order of 2 nm).

For proteins a variety of additional electronic excitations can be envisaged: delocalized electrons in amino acids with conjugated double bonds or electronic excitations along the peptide chain can add to the EEL spectra at low-energy loss. Such additional inelastic interactions could explain the more than two times higher filter contrast for protein embedded in ice compared to simple inorganic carbon films. To answer this question conclusively additional work on the EEL spectra of proteins and other organic polymers in the low loss region could be helpful. Such work has been done [3] but did not provide information for the region below an energy loss of 5 eV.

The actual inelastic scattering factor of atoms in organic molecules has not been calculated so far. This might even be impossible since the described molecular excitations cannot be modelled correctly. An interesting approach could be the exploitation of the EEL spectrum. If a direct correspondence between energy loss and delocalization of the inelastic scattering centre could be established for organic polymers, the inelastic scattering potential would follow directly from the EEL spectrum.

The observed dependence of the filter contrast on the energy window width of the filter aperture proves the importance of true zero-loss filtering. The inelastic scattering potential can only be interpreted as an absorption potential if all electrons that have lost energy are removed. With the present generation filters a wide energy window is needed to visualize a reasonable specimen area [35]. Thus, even in so-called zero-loss images, a considerable amount of inelastically scattered electrons is present, depending on the filter width and the shape of the EEL spectrum at low-energy loss.

The experimental data indicated problems with the new zero-loss CTF at very low resolution. The positions of the first zeros of CTFs from zero-loss images did not agree well with the theoretical CTF. This can be explained by an additional phase contrast contribution from inelastically scattered electrons that were not removed. However, such multiple scattering effects are very small and another explanation seems more likely: Up to now the filtering cannot remove all inelastically scattered electrons, and hence the recorded image is a superposition of the zero-loss image and the low loss part of the inelastic image. This inelastic contribution will alter the contrast in the image and

subsequently change the experimental contrast transfer function. It is not obvious how such a superposition will affect the positions of the zeros. Image simulations are planned to answer this question.

The new ansatz for the contrast formation now allows a more global description of image formation. An EM image is the superposition of the elastic and the inelastic image. The elastic image is formed by three scattering potentials, the elastic phase and amplitude scattering potential and the inelastic scattering potential. In this ansatz image formation includes the additional filter potential in contrast to the conventional theory where the elastic image is formed by phase and amplitude contrast only.

In an EFTEM a true zero-loss image corresponds to the elastic image. In a conventional TEM these images cannot be separated. Therefore, unfiltered images will have certain contrast artefacts if the inelastic image contrast cannot compensate the filter contrast. Such an image will then be a superposition of the conventional elastic image and some mixture of inelastic contrast. The use of an EM that minimizes chromatic aberration effects will minimize these superposition artefacts, as illustrated by data from a 300 keV EM with small chromatic aberration. Such data can be described quite well by the conventional elastic phase and amplitude theory.

Our results show that by removing inelastically scattered electrons the EFTEM not only reduces the inelastic noise contribution in images, but in addition it increases signal in the elastic image. This signal enhancement results from an additional amplitude contrast component. Even though it seems that this "filter contrast" does not extend to quasi-atomic resolution for typical biological samples, the resulting improved specimen visibility is most important for samples with weak contrast such as biological macromolecules embedded in ice. Studies with the actin–myosin complex demonstrated that even with a small number of zero-loss filtered images a resolution of about 2 nm can be obtained. Furthermore, a quantitative object reconstruction, i.e. a reconstruction with corrected amplitudes of the structure factors at all spatial frequencies, was possible.

Acknowledgements

The authors thank K.C. Holmes for continuous support and many helpful discussions and W. Jahn for contributing the biochemistry on the actin-myosin complex and for micrographs of that sample. The simulation program YaMS was provided by the Institute for Electron Optics, TU Darmstadt, and the authors would like to thank H. Müller, P. Schorsch, and H. Rose for help with the program and the discussion meetings in Heidelberg and Darmstadt. Some of the experiments were done at the EM facilities of the MPI for Biophysics in Frankfurt (Main), Germany, and the authors would like to thank W. Kühlbrandt for his support and D. Mills for his help at the JEOL SSF3000. This work was supported by the Deutsche Forschungsgemeinschaft (Schr 424/1-2).

References

[1] P.N.T. Unwin, R. Henderson, J. Mol. Biol. 94 (1975) 425.
[2] J. Dubochet, M. Adrian, J.-J. Chang, J.-C. Homo, J. Lepault, A.W. McDowell, P. Schultz, Quart. Rev. Biophys. 21 (1988) 129.
[3] S. Sun, S. Shi, R. Leapman, Ultramicroscopy 50 (1993) 127.
[4] R. Grimm, D. Typke, M. Bärmann, W. Baumeister, Ultramicrocsopy 63 (1996) 169.
[5] I. Angert, C. Burmester, C. Dinges, H. Rose, R.R. Schröder, Ultramicroscopy 63 (1996) 181.
[6] A. Harscher, H. Lichte, J. Mayer, Ultramicroscopy 69 (1997) 201.
[7] B. Feja, U. Aebi, J. Microscopy 193 (1999) 15.
[8] R. Grimm, H. Singh, R. Rachel, D. Typke, W. Zillig, W. Baumeister, Biophys. J. 74 (1998) 482.
[9] R. Henderson, J.M. Baldwin, T.A. Ceska, F. Zemlin, E. Beckmann, K.H. Downing, J. Mol. Biol. 213 (1990) 899.
[10] W. Kühlbrandt, D.N. Wang, Nature 350 (1990) 130.
[11] E. Nogales, S.G. Wolf, G. Downing, Nature 391 (1998) 199.
[12] H. Stark, F. Müller, E.V. Orlova, M. Schatz, P. Dube, T. Erdemir, F. Zemlin, R. Brima-combe, M. van Heel, Structure 3 (1995) 815.
[13] J. Frank, J. Zhu, P. Penczek, Y. Li, S. Srivastava, A. Verschoor, M. Rademacher, R. Grassucci, R.K. Lata, R.K. Agrawal, Nature 376 (1995) 441.
[14] R. Castaing, C.R. Acad, Sci. Paris 255 (1962) 76.
[15] W. Egle, A. Rilk, F.P. Ottensmeyer, Proceedings of the 8th European Congress on Electron Microscopy, 1984, p. 63.
[16] J. Trinick, J. Berriman, Ultramicroscopy 21 (1987) 393.
[17] R.R. Schröder, W. Hofmann, J.-F. Ménétret, J. Struct. Biol. 105 (1990) 28.

[18] J.P. Langmore, M.F. Smith, Ultramicroscopy 46 (1992) 349.
[19] R.R. Schröder, D. Manstein, W. Jahn, J.A. Spudich, Proceedings of the 51st Annual Meeting of the Microscopy Society of America 1993, p. 118.
[20] J. Zhu, P. Penczek, R.R. Schröder, J. Frank, J. Struct. Biol. 118 (1997) 197.
[21] H. Kohl, Ultramicroscopy 16 (1985) 265.
[22] H. Kohl, H. Rose, Adv. Electr. Phys. 65 (1985) 173.
[23] I. Angert, W. Jahn, K.C. Holmes, R.R. Schzöder, Proceedings of the 14th International Congress on Electron Microscopy, 1998, p. 683.
[24] C. Toyoshima, N. Unwin, Ultramicroscopy 25 (1988) 279.
[25] C. Toyoshima, Ultramicroscopy 48 (1992) 349.
[26] H. Mueller, R. Rose, P. Schorsch, J. Microscopy 190 (1998) 73.
[27] M.M.G. Barfels, Xungao Jiang, Yew Meng Heng, A.L. Arsenault, F.P. Ottensmeyer, Micron 29 (1998) 97.
[28] B. Freitag, W. Mader, Proceedings of the 14th International Congress on Electron Microscopy, 1998, p. 221.
[29] H. Rose, Optik 45 (1976) 139.
[30] H. Rose, Optik 45 (1976) 187.
[31] M. Isaacson, J.P. Langmore, H. Rose, Optik 41 (1974) 92.
[32] D.A. Muller, J. Silcox, Ultramicroscpy 59 (1995) 195.
[33] J. Zhu, J. Frank, Proceedings of the 13th International Congress on Electron Microscopy, 1994, p. 465.
[34] R.H. Wade, Ultramicrocopy 46 (1992) 145.
[35] S. Uhlemann, H. Rose, Optik 96 (1994) 163.
[36] W. Jahn, J. Microscopy 179 (1995) 333.
[37] P. Bele, R. Ochs, I. Angert, R.R. Schröder, Microscopy Research and Technique, in press.
[38] J. Frank, I. Shimkin, H. Dowse, Ultramicroscopy 6 (1981) 343.
[39] J. Frank, M. Radermacher, P. Penczek, J. Zhu, Yh. Li, M. Ladjadj, A. Leith, J. Struct. Biol. 116 (1996) 190.
[40] P.D. Welch, IEEE Trans. Audio Electroacoust. AU-15 (1967) 70.
[41] L. Reimer, Transmission Electron Microscopy, Springer, New York, 1990.
[42] P. Schiske, Proceedings of the 14th European Conference on Electron Microscopy, 1968, p. 145.